Research papers

Interannual variability of the subtropical countercurrent eddies in the North Pacific associated with the Western-Pacific teleconnection pattern

CrossMark

Chun Hoe Chow[a,d], Yu-heng Tseng[b,*], Huang-Hsiung Hsu[a], Chih-Chieh Young[c]

[a] Research Center for Environmental Changes, Academia Sinica, Taiwan
[b] Climate and Global Dynamics Division, National Center for Atmospheric Research, United States
[c] Hydrotech Research Institute, National Taiwan University, Taiwan
[d] Department of Oceanography, National Sun Yat-sen University, Taiwan

ABSTRACT

The connection and the relevant dynamical processes between oceanic eddies in the North Pacific Subtropical Countercurrent (STCC) region and the atmospheric Western-Pacific (WP) teleconnection is investigated on interannual timescales. North of the STCC region, the local northerly surface wind anomalies cool the ocean surface during negative phases of the WP teleconnection. The local surface cooling modifies the meridional gradient of sea surface temperature (SST), strengthening the SST front at its south. In the STCC region, we show the meridional gradient of surface-heat-flux forcing caused by the local surface cooling is the same order as the Ekman-convergence forcing. The strengthened SST front then leads to the pycnocline shoaling in the STCC region, which can also enhance the growth of baroclinic instability to produce more oceanic eddies, in addition to the enhanced STCC proposed previously. These dynamics are reversed during the positive phases of WP teleconnection.

1. Introduction

The variability of oceanic eddies in the North Pacific Subtropical Countercurrent (STCC) region has drawn much attention over the last decades (Qiu, 1999; Roemmich and Gilson, 2001; Hwang et al., 2004; Qiu and Chen, 2005; Qiu and Chen, 2010; Chow and Liu, 2012; Yang et al., 2013). Based on satellite observations, the eddy signature reflected by sea surface height (SSH) variation has a dominant time scale of about 100 days and a dominant eddy wavelength of about 800 km along the STCC band (Liu and Li, 2007; Qiu and Chen, 2010). The number of anticyclonic eddies is larger than that of cyclonic eddies by about 16.9% (Yang et al., 2013) climatologically. The eddies, which are most active in spring (Qiu, 1999), typically move westward at a speed of about 0.1 m/s due to the planetary beta effect (Cushman-Roisin et al., 1990; Hwang et al., 2004; Lin et al., 2006).

The westward moving eddies can interact with the Kuroshio when approaching Taiwan, modulating Kuroshio transport and path (Yang, 1999; Zhang et al., 2001; Yuan et al., 2006; Shen et al., 2014; Chow et al., 2015). They can affect the local circulation in the South China Sea after penetrating through the Luzon Strait when the Kuroshio becomes weak during fall and winter (Sheu et al., 2010). They also transport heat northward via meridional advection in the subtropical North

Pacific (Roemmich and Gilson, 2001; Qiu and Chen, 2005). The warm and cold sea surface temperature (SST) tongues formed by the meridional advection could influence ocean wind variability (Small et al., 2005; Chow and Liu, 2012).

During its negative phases, the pattern of the atmospheric Western-Pacific (WP) teleconnection consists of a north-south dipole of 500-hPa geopotential height anomalies (H500 anomalies), with the northern lobe of positive anomalies located over the Kamchatka Peninsula and another broad southern lobe of opposite sign covering portions of southeastern Asia and the western subtropical North Pacific (Fig. 1) (Wallace and Gutzler, 1981). The eddies in the North Pacific STCC region are active in some years, corresponding to the negative phases of the WP pattern (referred to "WP teleconnection pattern" hereafter) on interannual timescales (Qiu and Chen, 2010; Shen et al., 2014). The eddy strength is mainly determined by the vertical shear between the eastward-flowing STCC and the subsurface westward-flowing North Equatorial Current (NEC). When the STCC flows faster, larger vertical shear increases the baroclinic instability of the STCC-NEC system, potentially forming more eddies (Qiu and Chen, 2010). The STCC resides below the southern boundary of the WP-pattern southern lobe (Fig. 1; box centered at about 22°N approximately shows the region of STCC). Qiu and Chen (2010) show that the surface winds associated
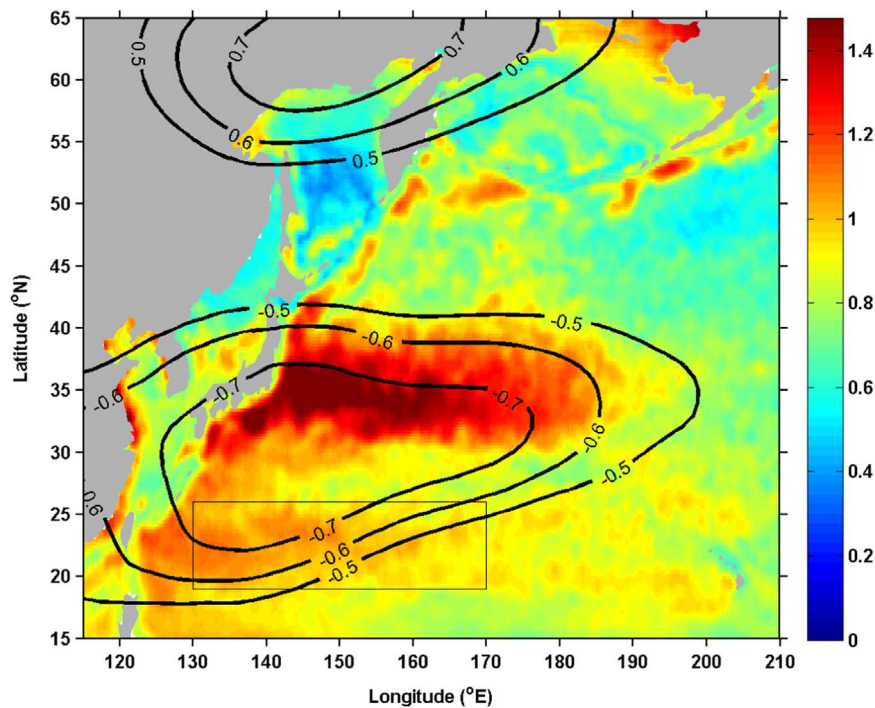

Fig. 1. The normalized standard deviation of SSH anomalies from altimetry observation (colors) from 1993 to 2010, superimposed with the negative phase of WP pattern (selected contours), during December to following April from 1993 to 2010. The standard deviation values shown are natural logarithm. The WP pattern is shown by the correlation between the WP index provided by the Climate Prediction Center (CPC) and the geopotential height at 500 hPa provided by the European Center for Medium-Range Weather Forecasts (ECMWF). The box centered at about 22°N shows the region of interest within 130° to 170°E and 19° to 26°N. (For interpretation of the references to color in this figure legend, the reader is referred to the web version of this article.).

with the negative phases of WP pattern increase Ekman convergence at the surface in the subtropics and then strengthen the STCC, modulating the interannual variability of the STCC and eddies. On interannual to decadal timescales, the forcing of Ekman convergence and surface heat flux is important for eddy variability in the region (Qiu and Chen, 2013). The Kuroshio transport east of Taiwan can be altered significantly by the interannually varying eddies (Yang, 1999; Zhang et al., 2001) related to the WP pattern (Shen et al., 2014).

This paper aims to clarify the dynamical processes linking these eddies and the WP pattern on interannual timescales by answering the following scientific questions: (1) How are the anticyclonic and cyclonic eddies connected with the atmospheric variability; (2) What are the other key factors controlling the state and variability of eddies in addition to the increase of STCC flow speed suggested in Qiu and Chen (2010); and (3) How are these key factors influenced by the WP pattern? It is found that these eddies vary with the WP pattern under circumstances of steep thermocline tilt in the subtropics (Qiu and Chen, 2010; Shen et al., 2014). We hypothesize that, besides the STCC flow speed, the variability of pycnocline depth, which to date was not a focus for the eddy-activity issue, may play an important role to enhance the growth of baroclinic instability and eddies in the STCC region. Thus, the surface-wind variability modulated directly by the WP pattern alters the background SST gradient field via surface heat flux and Ekman convergence, resulting in changes of pycnocline depth leading to the observed interannual variability of eddy fields. Moreover, this paper also investigates the atmospheric variability from the surface up to the 500-hb height, corresponding to the eddy activity, thus completing the dynamical processes linking the WP pattern defined at the 500-hb height to eddies at the surface.

Section 2 describes the methodology and data used. Section 3 shows the STCC eddy bands, followed by the discussion of the oceanic interannual variability related to the WP pattern in Section 4. Section 5 details the heat-flux process linking the eddy interannual variability to that of WP pattern. Finally, results are discussed and summarized in Section 6.

2. Methodology

2.1. Observation and reanalysis

Monthly SSH-anomaly data is gridded at a 0.25° resolution from 1993 to 2010, distributed from the Archiving, Validation and Interpretation of Satellite Oceanographic data (AVISO) (Ducet et al., 2000). To study the ocean vertical structure, we used the temperature and salinity (TS) profiles of "EN3_v2a" monthly 1° objective analysis dataset from 1993 to 2010 (Guinehut et al., 2009), provided by the Met Office Hadley Center. The EN3_v2a reanalysis is mainly based on the data of Argo and Global Temperature and Salinity Profile Project (GTSPP).

The TS profiles of EN3_v2a are then used to estimate the buoyancy frequency (N^2) at approximately 0–540 m depth and 23.8-sigma depth to represent the shallow upper-layer variability. The buoyancy frequency was estimated from:

$$N^2 = -\frac{g}{\rho_0}\frac{\partial \rho}{\partial z}, \tag{1}$$

where $\frac{\partial \rho}{\partial z}$ is the density vertical gradient, ρ_0 is the reference density and g is the gravity. The 23.8-sigma surface was chosen because it resides at the depth varying between 50 and 95 m, slightly below the mixed layer depth at about 50 m (Qu, 2003). This sigma surface reasonably estimates the shallow upper-layer thickness variability.

To analyze the corresponding atmospheric variability, we used the monthly 1° dataset of the Interim Reanalysis of the European Center for Medium-Range Weather Forecasts (ECMWF) (Dee et al., 2011). The surface wind stress and SST data from the ECMWF Interim Reanalysis were mainly used to estimate the "Ekman-convergence forcing" and "heat-flux forcing" defined in Section 2.2. We also used the atmospheric dataset of geopotential height, air temperature, specific humidity and wind vectors from 500 hPa to 1000 hPa, and the surface dataset of pressure, sensible heat flux and latent heat flux from the
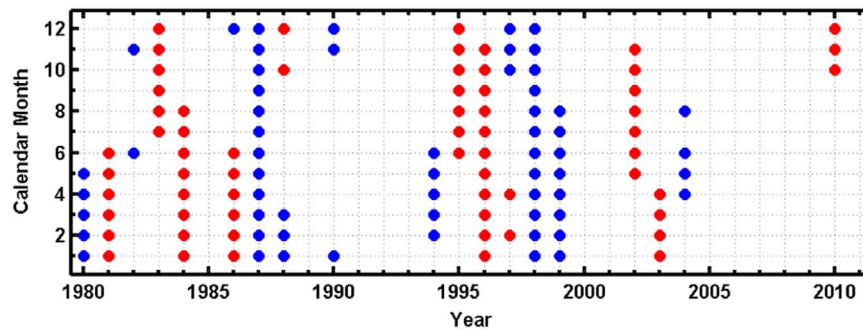
Fig. 2. Calendar months with negative (red dots) and positive (blue dots) phases of WP pattern. (For interpretation of the references to color in this figure legend, the reader is referred to the web version of this article.).

ECMWF Interim Reanalysis to study the atmospheric variability corresponding to the eddy activity.

The WP-pattern index was obtained from the Climate Prediction Center (CPC) of the National Oceanic and Atmospheric Administration (NOAA). A 13-month running mean was applied to the WP-pattern index for interannual timescales. Then, the positive and negative phases of the WP pattern were defined when the index's absolute value was larger than one standard deviation (std). Fig. 2 shows the calendar months with negative and positive phases of WP pattern applied for the composite analysis in this study.

2.2. Eddy kinetic energy, Ekman-convergence forcing and heat flux forcing

The observed "eddy kinetic energy" (EKE) associated with each eddy was estimated using the altimetry SSH anomaly data. It was defined as $(u_g'^2 + v_g'^2)/2$, where u_g' and v_g' are the anomalies of zonal and meridional geostrophic velocities, respectively, estimated from the Coriolis (f) and pressure balance of SSH anomalies (Hwang et al., 2004). To study the SST front variability, a frontogenesis equation may be written as (Nakamura and Kazmin, 2003):

$$\frac{\partial G}{\partial t} \approx -\frac{\partial (V_E \cdot G)}{\partial y} + \frac{\partial (Q/\rho Ch)}{\partial y}, \tag{2}$$

where G is the meridional SST gradient (i.e., $-\partial T/\partial y$), assuming that it corresponds to the thermocline tilt and can be used as a proxy to study the interannual variability of thermocline tilt. The first and second terms on the right-hand side are the forcing of Ekman convergence and heat flux, respectively. The V_E in the first term is the meridional Ekman velocity given as $V_E = \tau_x/\rho fh$, τ_x is the zonal wind stress, ρ is the reference density, and h (=150 m) is the thickness of the surface layer (Qiu and Chen, 2010). The heat flux term Q represents the net upward surface heat flux and C is the seawater specific heat at constant pressure. Here, the geostrophic-advection term is neglected because its order is much smaller than that of the Ekman advection (Qu, 2003). Furthermore, the entrainment and residual forcings are omitted for simplicity. To compute these two terms, Eq. (2) is rewritten in its integral form as follows (Qiu and Chen, 2013):

$$G \approx -\int_{t_1}^{t_2} \frac{\partial (V_E \cdot G)}{\partial y} dt + \int_{t_1}^{t_2} \frac{\partial (Q/\rho Ch)}{\partial y} dt. \tag{3}$$

where the two terms on the right-hand side, having the same order of magnitude (Roden, 1975), are important processes contributing to the variability of the subtropical front (Roden, 1975; Kazmin and Rienecker, 1996) and STCC (Qiu and Chen, 2010; Qiu and Chen, 2013) in the North Pacific. The first term is caused by westerlies in the north and trades in the south. The second term is contributed by the net surface heat flux.

3. STCC Eddy bands

The SSH variability along the 22°N latitude in the western North Pacific increases to the west (Liu and Li, 2007; Qiu and Chen, 2010), showing clear eddy activity. Generated by the baroclinic instability (Qiu and Chen, 2010) these eddies commonly move westward (Hwang et al., 2004) in the STCC region and then impinge on the Kuroshio off the east coast of Taiwan (Yang, 1999), significantly modifying the Kuroshio transports (Yang, 1999; Zhang et al., 2001; Vélez-Belchí et al., 2013; Shen et al., 2014).

Fig. 3 shows the absolute values of the positive and negative SSH anomalies averaged from January 1993 to December 2010. Only those grids and times with positive SSH anomalies are taken into account for the results shown in Fig. 3a. Similarly, Fig. 3b only takes those with negative SSH anomalies into account. The zonal eddy bands are identified from the large positive and negative SSH anomalies centered at about 24°N (Fig. 3a) and 21°N (Fig. 3b), respectively. The numbers of anticyclonic and cyclonic eddies based on the global "mesoscale-eddy" trajectories dataset (Chelton et al., 2011) are superimposed as contours on Fig. 3. Note, only those eddies with amplitude greater than 10 cm are taken into account (Chelton et al., 2011). The spatial distribution of eddy numbers is similar to the corresponding SSH anomalies, indicating the consistency between the SSH variability and eddy number.

These two eddy zonal bands are evident in the differences of the absolute values between the positive and negative SSH anomalies (Fig. 3c), which show that anticyclonic (cyclonic) eddies are dominant in the regions with larger (smaller) f in the north (south) (Cushman-Roisin and Beckers, 2008). Overall, these features are also observed in the std of SSH anomalies (Fig. 1). We can see a region of large SSH anomalies roughly within 130° to 170°E and 19° to 26°N (the region of interest in this study), excluding the Kuroshio region extending from the Taiwan coast to about 123.5°E between 22° and 25°N (Hsin et al., 2008).

In the STCC region, the signatures for anticyclonic (Fig. 3a) and cyclonic (Fig. 3b) eddies are generally amplified from east to west. The number for both anticyclonic and cyclonic eddies becomes approximately 25 to 27% larger within 130° to 150°E than within 150° to 170°E. Overall, the number of anticyclonic eddies are about 12% more than that of cyclonic eddies within 130° to 170°E, consistent with the previous findings of Yang et al. (2013), which indicates that the number of anticyclonic eddies is about 16.9% greater than the cyclonic eddies in a larger domain (122° to 170°E and 12° to 28° N).

4. Interannual variability of eddies related to upper-layer thickness

The time-series of the normalized EKE in our region of interest is shown in Fig. 4 (black curve). The EKE is large (> 0) in 1995 to 1998, 2001 and 2003–2006, but small (< 0) in 1999 to 2000, 2002, 2007 and 2009. We also superimpose the numbers of anticyclonic (red curve)
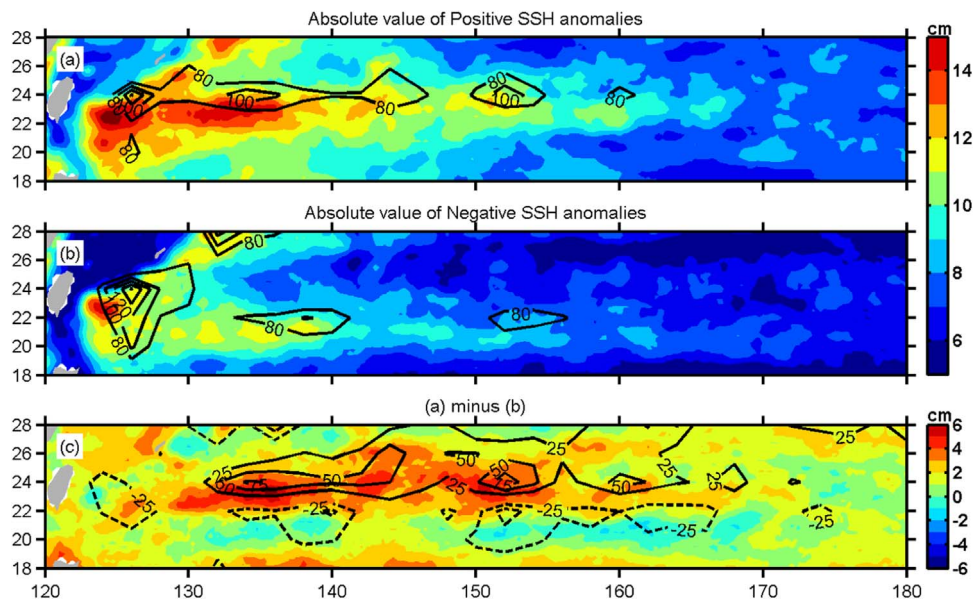
Fig. 3. (a) Absolute value of the positive SSH anomalies (colors) and the anticyclonic-eddy numbers (contours), averaged from January 1993 to December 2010 based on satellite altimeter data. (b) Same as (a) but for the negative SSH anomalies and cyclonic-eddy numbers. (c) The difference between (a) and (b). (For interpretation of the references to color in this figure legend, the reader is referred to the web version of this article.).

and cyclonic (blue curve) eddies based on the datasets of "mesoscale-eddy" trajectories (Chelton et al., 2011). As expected, the EKE correlates well with the number of anticyclonic and cyclonic eddies with coefficients of about 0.89 and 0.72, respectively. This small difference in coefficient might be due to the small difference in number of anticyclonic and cyclonic eddies, as given in Section 3. Thus, both EKE and eddy number increase when the background STCC strengthens. Importantly, Fig. 4 also shows the time series of buoyancy frequency (N^2), 23.8-sigma depth and WP index. The EKE lags the N^2, 23.8-sigma depth and WP index by about 11–13 months with a coefficient of about 0.70, 0.53 and 0.58, respectively. The N^2 significantly correlates with the WP pattern. It also correlates well with 23.8-sigma depth without any lag. This correlation analysis suggests that during the negative phases of WP pattern, the 23.8-sigma depth and N^2 decrease in response to the change of WP, leading to the growth of instability and more eddies one year later, which is the time that the eddies might need to fully grow and respond on the surface. These dynamics are reversed during the positive phases of WP pattern.

For two-layer baroclinic instability, the stable condition can be written as (Cushman-Roisin and Beckers, 2008):

$$|\Delta U| \leq 2\beta_0 R^2, \tag{4}$$

where ΔU is the velocity shear between two layers, β_0 is the meridional gradient of the Coriolis parameter at a reference latitude and R is the baroclinic radius of deformation, which is the function of buoyancy

frequency and layer thickness. That implies the system can be stable for all small perturbations when ΔU does not exceed $2\beta_0 R^2$ theoretically and can be unstable when ΔU becomes larger or R^2 becomes smaller until the condition breaks. Thus, in addition to the STCC strengthening that directly increases the velocity shear suggested by Qiu and Chen (2010, 2013), the decreasing of upper layer thickness can also enhance the growth of baroclinic instability through the reduction of N^2 and subsequent decrease of the deformation radius R.

To demonstrate the role of the upper layer thickness in the eddy variability, Fig. 5 shows the time-longitude plots of EKE, eddy number and 23.8-sigma depth anomalies averaged within 19–26°N region during March to May (season with active eddies in the STCC region) at one-year resolution. Both EKE and the number of eddies generally increase to the west and reach their maxima within 130–150°E. Most importantly, they are mostly large when the 23.8-sigma depth decreases, suggesting that the shallow upper layer variability may play a key role in determining the eddy interannual variability in the STCC region. The interannual variability of the 23.8-sigma depth (Fig. 5b) changes more than 40 m on average, about 54% of its mean depth at about 74 m in the STCC region, exhibiting the significant variation of the shallow upper layer.

Fig. 6 shows the averaged vertical density gradient along the zonal and meridional sections in spring. Based on the maximum vertical density gradient, two pycnoclines are clearly seen at difference depths. The upper pycnocline is roughly along the 23.8-sigma surface at about
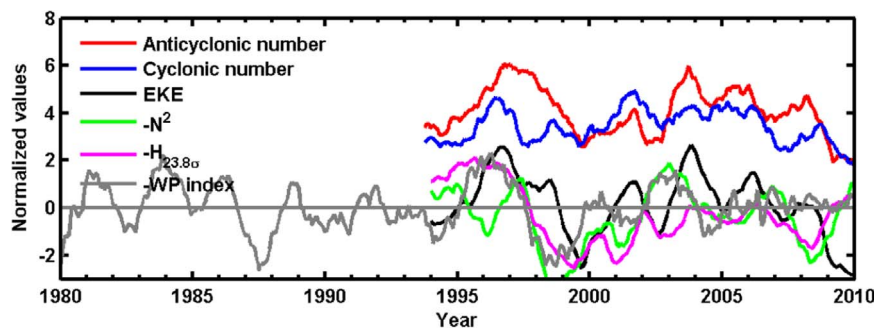

Fig. 4. Monthly time series of eddy numbers (red for anticyclonic, blue for cyclonic), normalized EKE anomalies (black), normalized buoyancy-frequency anomalies (green, negative), normalized 23.8-sigma depth anomalies (magenta, negative) in the region of interest from altimetry observations and that of negative WP index (gray). A 13-month moving average was applied. (For interpretation of the references to color in this figure legend, the reader is referred to the web version of this article.).
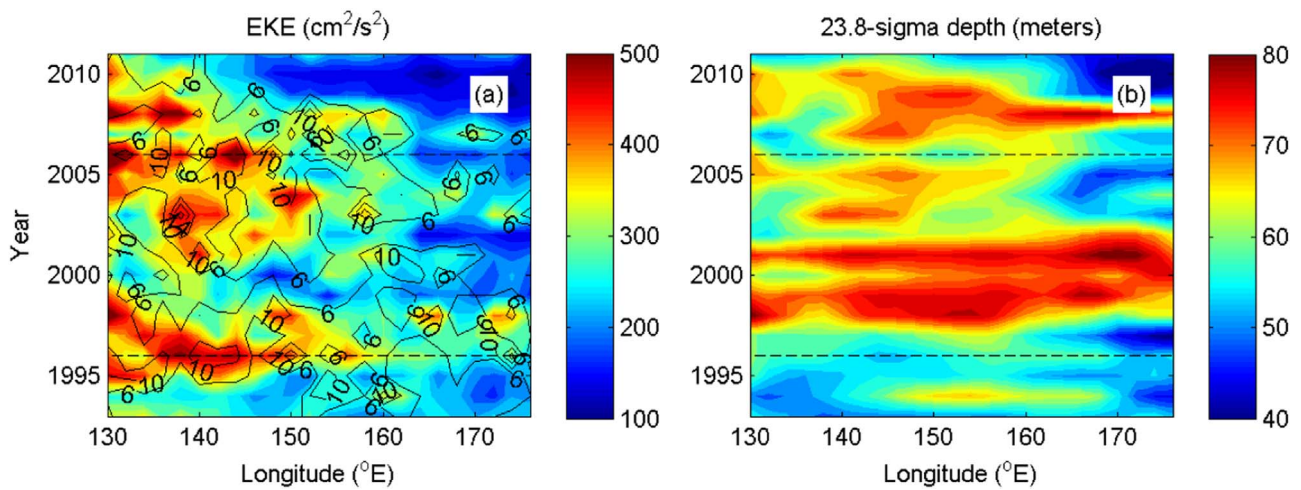
Fig. 5. Time-longitude plot of (a) EKE, eddy numbers (contours) and (b) 23.8-sigma depth. Values shown are the averages within 19–26°N during March to May. The dashed lines indicate 1996 and 2006. (For interpretation of the references to color in this figure, the reader is referred to the web version of this article.).

50 m depth. The other lower pycnocline is located around 150 m depth, above the 25.5-sigma surface. For the upper pycnocline, the largest vertical density gradient in spring is generally in the west (Fig. 6a) and north (Fig. 6b) of the STCC region, thus shoaling the upper layer. On interannual timescales, the 23.8-sigma depth is shallower (deeper) during the years of more (less) active eddies when the EKE is greater (weaker) than one std, shown as the red (blue) solid lines. This feature cannot be found in the 25.5-sigma surface and suggests that the 23.8-sigma depth changes, considered as shallow upper-layer thickness changes, may be an important key to determine the interannual variability of eddies in the STCC region.

5. Impacts of the WP pattern via surface heat flux

Why does the 23.8-sigma surface shoal in the STCC region during the eddy-rich years? Qiu and Chen (2010) suggested that the Ekman convergence, which corresponds well with the interannually varying negative WP index, acts to maintain the thermocline tilt of the STCC against other frontolysis processes. This is consistent with the shoaling of 23.8-sigma during the negative phase of the WP pattern. The

extensively negative contours in the difference between the negative and positive phases (Fig. 7) further confirm that the 23.8-sigma surface tends to be shallower during negative phases of the WP pattern as well.

The Ekman convergence effectively increases the vertical shear (or, equivalently, the surface thermocline slope) of the STCC-NEC system to induce more eddies in the negative WP phase (Qiu and Chen, 2010). As mentioned in Section 4, the EKE significantly correlated with the negative WP index with a time lag of about 11 months. This is similar to the results of Qiu and Chen (2010) that the EKE lags the Ekman convergence forcing by 9 months. A slightly longer time is required for the STCC–NEC shear instability to fully grow and adjust in response to the time-varying Ekman forcing (Qiu and Chen, 2010). However, there is no one-to-one correspondence. For example, the low EKE occurs during 2009–2010 (Fig. 4) while the WP pattern is in the neutral phases. The correlation between the EKE and WP pattern becomes low after 2008. Some other dynamical processes may affect the EKE interannual variability in 2009 to 2010.

Besides the Ekman convergence, the surface heat flux can also change the variability of thermocline tilt in the STCC region through its contribution to the SST meridional gradient in Eq. (2). Fig. 8a shows
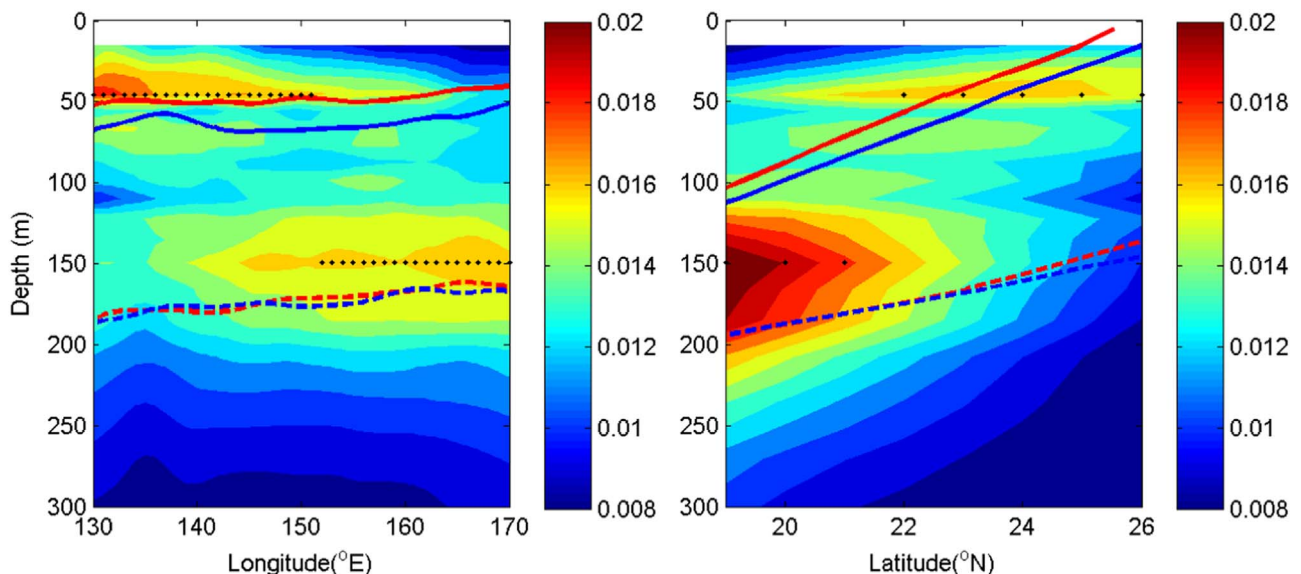

Fig. 6. Vertical gradient of density (kg/m⁴) averaged within (a) 19–26°N and (b) 130–170°E during March to May from 1994 to 2010. The red (blue) solid lines show the contours of 23.8 sigma when the EKE is greater (weaker) than one std, respectively. The dashed contours are the same but for the 25.5 sigma surface. The black dots show the depth of maximum vertical density gradient. (For interpretation of the references to color in this figure legend, the reader is referred to the web version of this article.).
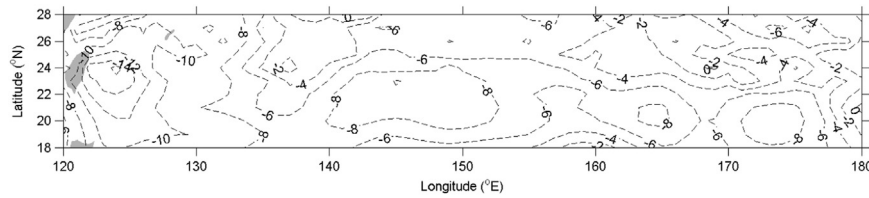
Fig. 7. Difference of 23.8-sigma depth (units: m) during the negative and positive phases of WP pattern (positive=solid line; negative=dashed line) from 1994 to 2010. A 13-month moving average was applied.

the 500-mb geopotential height anomalies (H500 anomalies), surface pressure and surface wind stress vectors averaged during the negative phases of WP pattern from 1980 to 2010. As expected, the anomalies of H500 and surface pressure manifest in a north–south oscillation, forming the anomalies of cyclonic surface wind within 25 and 50°N. Then, northerly wind anomalies are induced north of the STCC band, implying that the surface might be significantly cooled during the negative phases of WP pattern. The reversed dynamics are found during the positive phases of WP pattern (Fig. 8b).

In Fig. 9, in order to further examine the impact of the WP pattern on the western North Pacific, we show the anomalies of air temperature, geopotential height, specific humidity, wind vectors, SST, and surface heat flux averaged over the negative phases of WP pattern from 1980 to 2010 along a northeast-inclined vertical section (the bold gray line in Fig. 8). This section roughly links over the Kamchatka Peninsula with the northern lobe of the WP-pattern and the STCC region with active eddies. The geopotential height anomalies show the two lobes of the WP pattern. The air temperature is significantly lower than the average at the southern lobe of the WP pattern. The wind from the mid-troposphere at about 500 hPa brings down the cold air and then flows southward when approaching the surface, forming dry and cold northerly wind near the surface. The anomalies of SST and surface heat flux are relatively low within 20 and 35°N during the negative phases of the WP pattern. Note the heat flux is positively downward in the ECMWF datasets. Thus, the negative heat flux shown in Fig. 9c indicates ocean heat loss to the atmosphere, confirming that the surface is cooled via surface heat flux by the northerly wind anomalies. We can

argue that the decrease in SST can feedback and modify the low-level atmosphere. However, based on Wu et al. (2006), the latent heat flux is negatively correlated with the SST tendency in the STCC region, showing the dominant atmospheric forcing to the SST changes. All results are reversed for the positive phases of WP pattern (not shown).

How does the surface cooling determine the SST meridional gradient in response to the WP pattern? Based on Eq. (3), the surface heat-flux can also affect the variability of SST meridional gradient, in addition to the impact of Ekman convergence (Qiu and Chen, 2010; Qiu and Chen, 2013). We estimate the three-month integrated forcings of Ekman convergence and surface heat flux using the two right-hand side terms of Eq. (3), respectively, after the negative and positive phases of WP pattern (Fig. 10). The "three-month" here is selected arbitrarily to compare these two forcings after the occurrence of these two phases. Averaged over the region of 130–170°E and 19–26°N, the mean Ekman convergence and the mean surface heat flux are about 0.35×10^{-6} °C/m and 0.18×10^{-6} °C/m, respectively, during the negative phases of WP pattern. The comparable order of magnitude between the surface heat flux and the Ekman convergence indicates the noticeable role of the surface heat-flux. Interestingly, the mean Ekman convergence decreases significantly to about 0.19×10^{-6} °C/m during positive phases of the WP pattern while the mean surface heat flux is still 0.16×10^{-6} °C/m. The mean Ekman convergence drops about 46%, larger than that of the surface heat-flux, which is about 11%. This difference shows that, after a three-month integration, the Ekman convergence could have larger impacts on the SST meridional gradient than the surface heat-flux does between the negative and positive
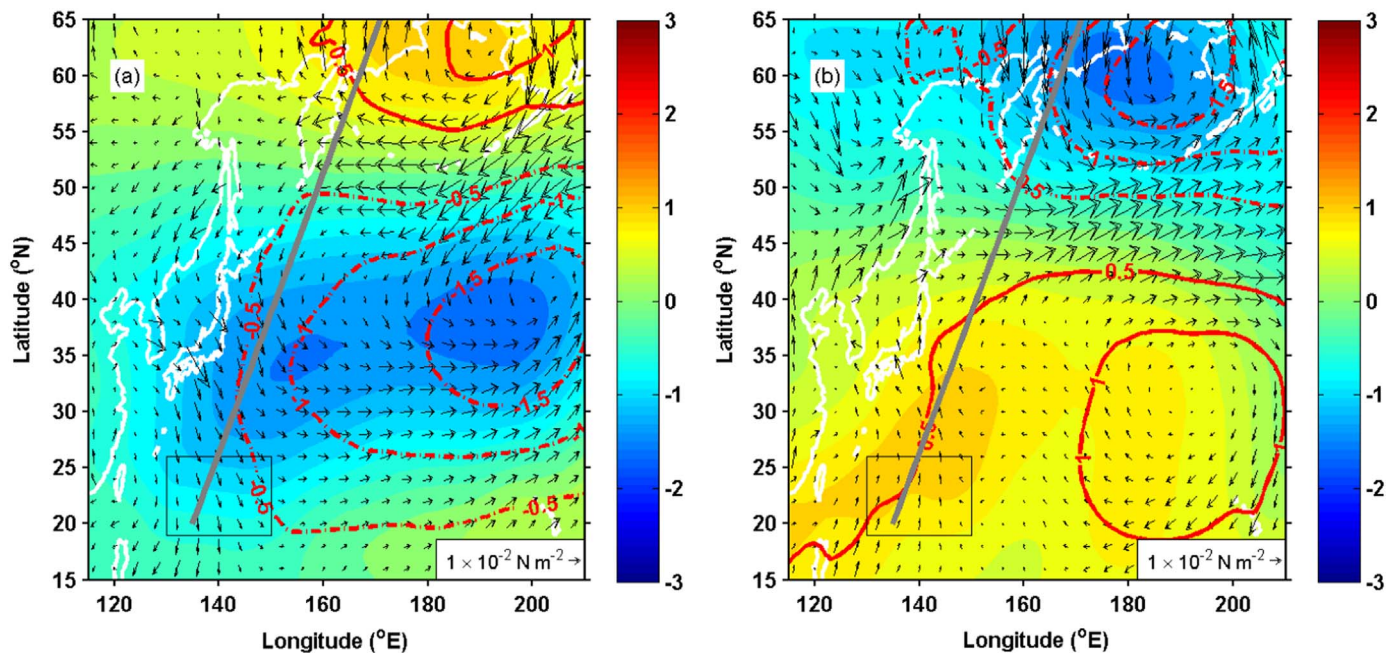

Fig. 8. (a) Anomalies of 500-hPa geopotential height (color shaded), surface pressure (selected contours) and surface wind stress vector (arrows) averaged during the negative phases of WP pattern from 1980 to 2010. (b) Same as (a) but during the positive phases of WP pattern. The geopotential height and surface pressure shown are normalized by their individual standard deviation along each latitude. The bold gray lines represent the vertical section shown in Fig. 9. A 13-month moving average was applied. (For interpretation of the references to color in this figure legend, the reader is referred to the web version of this article.).
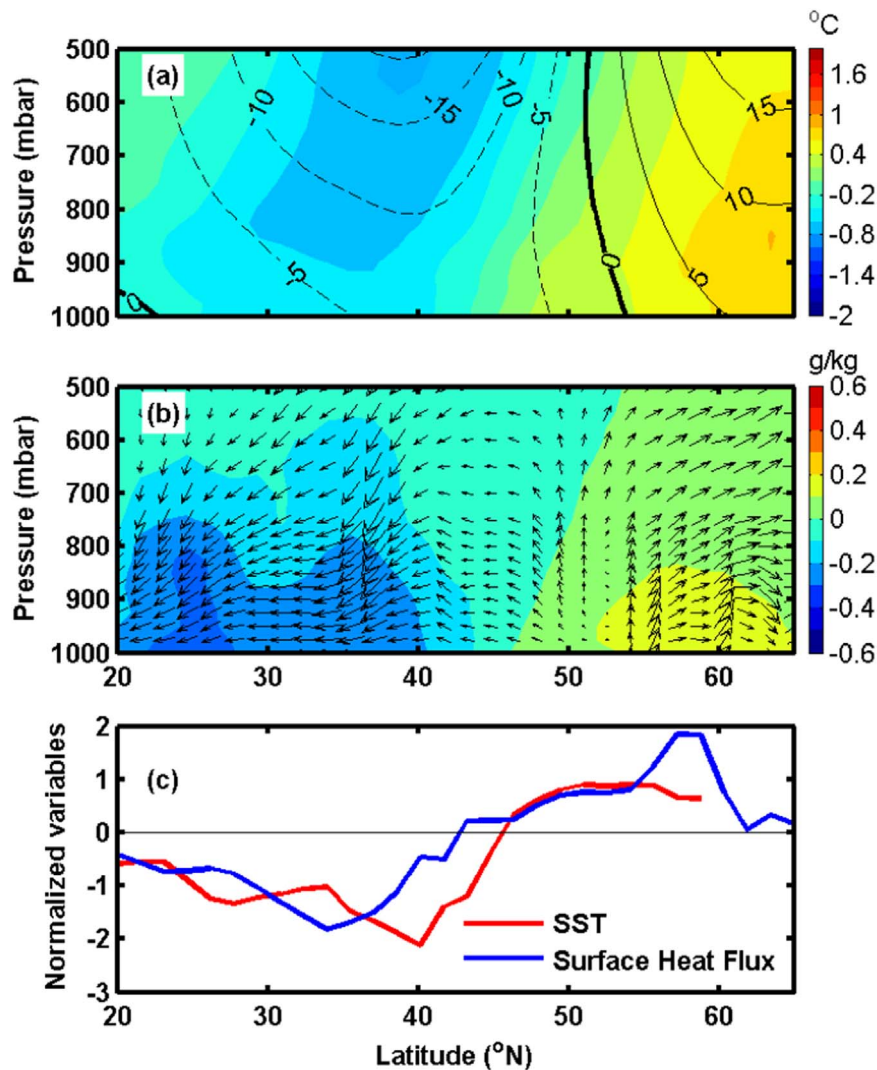
Fig. 9. Vertical section anomalies of (a) air temperature and geopotential height (contours, units: $\times 10$ m^2/s^2), (b) specific humidity and wind vectors, (c) SST and surface heat flux along the bold gray line shown in Fig. 8, averaged during the negative phases of WP pattern from 1980 to 2010. The variables in (c) and the v- and w-vectors of wind in (b) are normalized by standard deviation after removing the climatological monthly mean. A 13-month moving average was applied.

phases of WP pattern. However, what happens if a longer-time integration of Ekman convergence and surface heat-flux is analyzed?

We next compute the monthly time series of the SST meridional gradient (G), integrated Ekman convergence and integrated surface heat flux terms within the same region using Eq. (3). Following the work of Kobashi and Xie (2012), the integrated forcings of Ekman convergence and surface heat flux were computed for February and March (both winter and spring included) by setting t_2 to be either February or March and t_1 to be the previous August to March. The correlation coefficients between the changes of G and the integrated forcings in February or March are shown in Fig. 11. The coefficients at August of the t_1-axis correspond to the forcings integrated from August to February or March, while the coefficients at February correspond to the integration in February or integrated from February to March, and so on. The highest correlation in the circle curve shown in Fig. 11a occurs in January, indicating that the February SST meridional gradient G is significantly correlated with the Ekman convergence forcing integrated from January (t_1) to February (t_2), with a coefficient of about 0.56. The G in March (star curve in Fig. 11a) shows a weak but positive and significant correlation (within 0.35 and 0.5) with the integrated Ekman convergence forcing during winter (January to February), consistent with the analysis of Kobashi and Xie (2012). Our analysis of surface heat flux further shows that the G in March is

highly correlated with the heat-flux integrated from previous November (t_1) to March (t_2), with a high coefficient close to 0.70. While the SST gradient in February (circle curve in Fig. 11b) shows a weak but still positive and significant correlation (within 0.4 and 0.5) with the integrated heat flux forcing since the previous August to December. This analysis suggests that the interannual variability of the SST meridional gradient (G) in February and March is mainly controlled by Ekman convergence and surface heat flux, respectively, in response to the WP pattern.

6. Summary and concluding remarks

We investigated the connection between the oceanic eddies in the North Pacific STCC region and the atmospheric WP pattern on the interannual scales using satellite altimetry and reanalysis data. We confirm two eddy-rich zonal bands in the STCC region within 130 and 170°E: (1) the anticyclonic eddy-rich band within 22 and 26°N; and (2) the cyclonic eddy-rich band within 19 and 22°N (Fig. 3). The eddies are strengthened in years 1995–1998, 2001 and 2003–2006 (Fig. 4), lagging the 23.8-sigma surface shoaling by about one year (Fig. 5). This suggests that the shallow upper-layer thickness (represented by the water above the 23.8-sigma surface), which has not before been proposed, is another key factor controlling the state of eddies in the
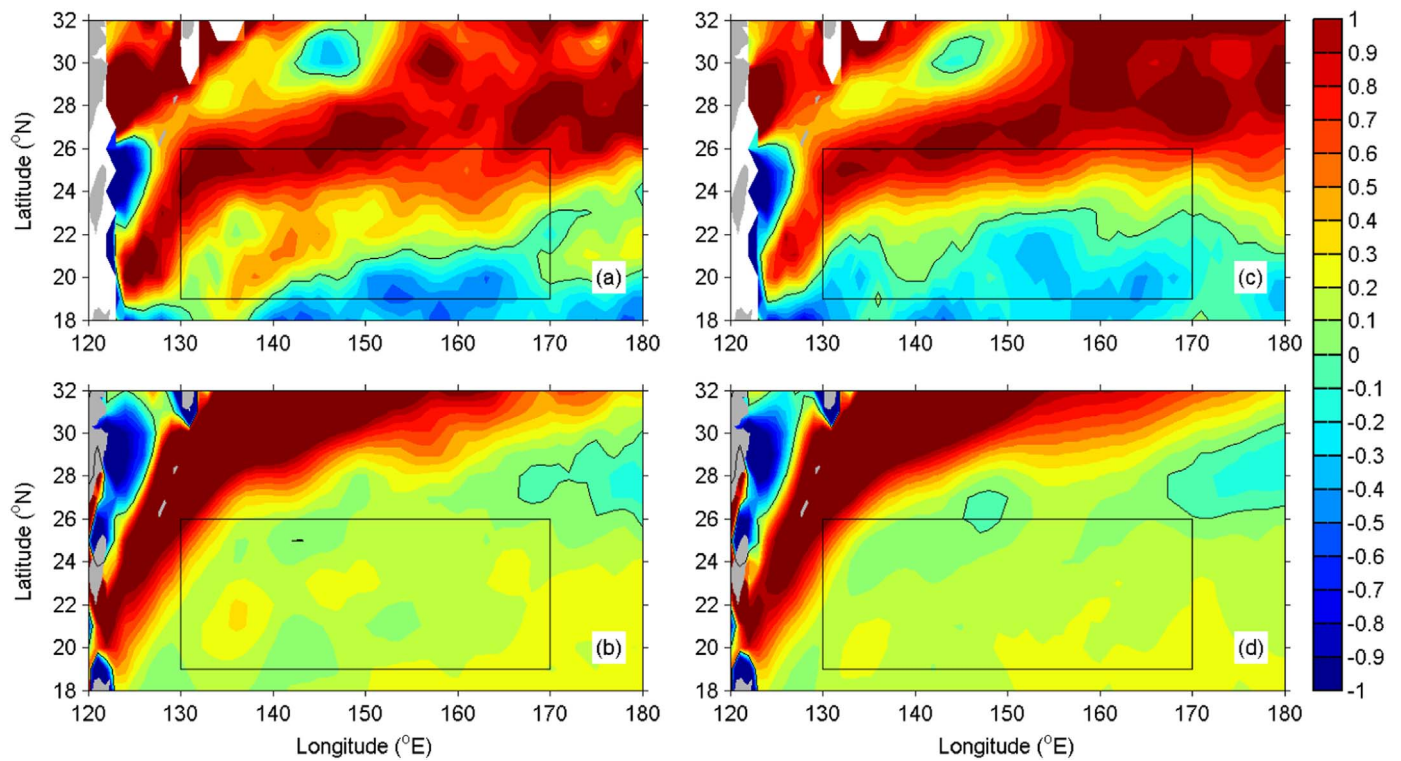
Fig. 10. Composite of (a) three-month integrated Ekman convergence forcing and (b) three-month integrated heat flux forcing after the negative phases of WP pattern from 1980 to 2010. (c) and (d) are the same as (a) and (b), respectively, but for the positive phases of WP pattern. All units are in 10^{-6} °C/m. (For interpretation of the references to color in this figure, the reader is referred to the web version of this article.).
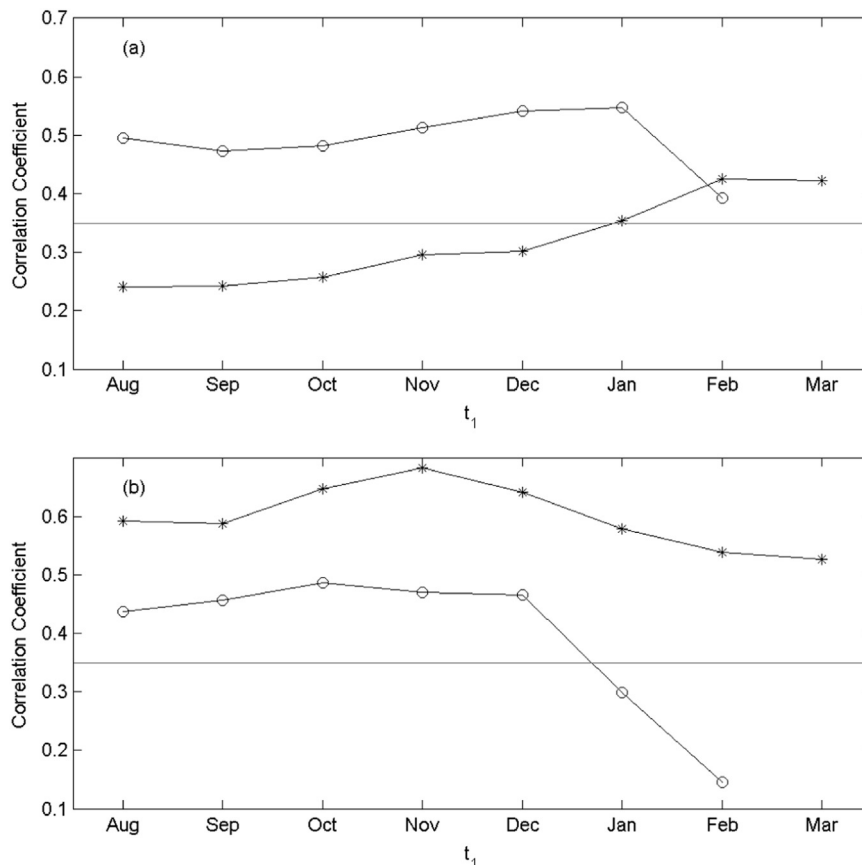

Fig. 11. (a) Correlation coefficients of the interannual variations of the meridional SST gradients (G) in February (circles) and March (stars) with Ekman convergence forcing integrated from t_1 to February (circles) and March (stars), respectively. Coefficients above the horizontal line are significant at the 95% confidence level. (b) Same as (a) but with heat flux forcing.
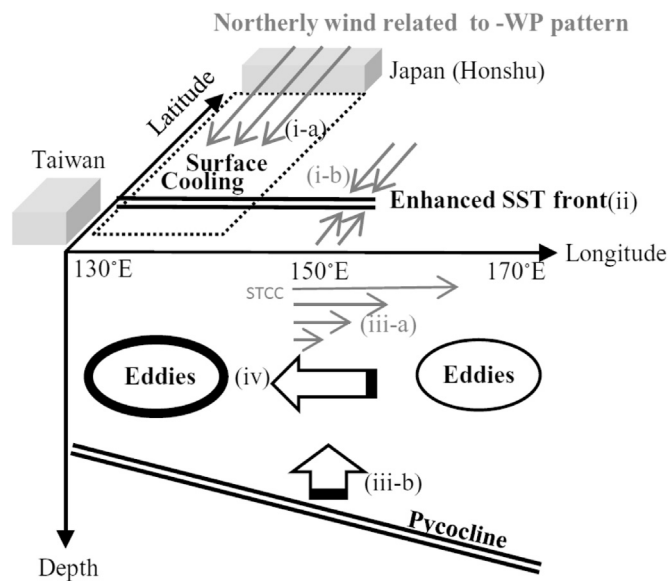
Fig. 12. Schematic diagram of the dynamical processes linking the interannual variability of STCC eddies and negative-phase WP pattern: (*i-a*) Northerly surface wind anomalies corresponding to the negative phases of WP pattern cool the local surface north of the STCC region; (i-b) Ekman convergence corresponding to the negative phases of WP pattern modified SST (Qiu and Chen, 2010); (ii) The SST front is enhanced in the STCC region; (iii-a) Vertical shear increased by the enhanced STCC causes instability and eddies (Qiu and Chen, 2010). (iii-b) Pycnocline raises and upper layer shoals, also favorable for instability and eddies to grow; (iv) Eddies are generally also strengthened when they move westward into a shallower upper-layer region.

STCC region besides the STCC strengthening, based on the stability criteria for baroclinic instability (Eq. (4)).

The impact of the WP pattern on the STCC eddies was further assessed and the dynamical processes linking the WP pattern to the north–south tilting of thermocline were clarified through changes in SST meridional gradient, which was assumed to correspond to the thermocline-tilt variability on the interannual scales. During negative phases of WP pattern, increased Ekman convergence forcing enhances the thermocline tilting as expected (Qiu and Chen, 2010). This leads to a shallower 23.8-sigma surface (considered as upper-layer variability) in the STCC region during the negative phases of the WP pattern compared to the positive phases (Figs. 6 and 7). The linear instability analysis suggests that the shallowing of the 23.8-sigma surface can also favor eddy growth. Thus, the eddies are more active during negative phases of the WP pattern than during the positive phases due to the combination of upper-layer shoaling and the vertical-shear strengthening. Moreover, eddies are also strengthened when moving westward into a region with a shallower upper layer (Fig. 7).

Our analysis further shows that, during negative phases of the WP pattern, the surface heat flux forcing, in the same order of magnitude as the Ekman convergence forcing, also significantly contributes to the SST meridional gradient on interannual timescales (Figs. 10 and 11). The surface heat flux is initiated by the surface northerly wind anomalies (Fig. 9) resulting from the downwelled winds in the mid-troposphere (approximately 500 hPa) at about 40°N. The winds bring down cold air, which then turn southward at the surface (Fig. 9) to cool down the ocean surface through surface heat flux change. This is consistent with the observed distributions of SST and heat flux anomalies. The surface heat-flux meridional gradient enhances the SST gradient and thus the thermocline tilting in the STCC region. All results are reversed during the positive phases of WP pattern.

The complete dynamical process linking the interannual variability of STCC eddies and the WP pattern is summarized in Fig. 12. During negative phases of WP pattern, defined at the 500-hb height, the local northerly surface wind anomalies cool the surface north of the STCC region (Fig. 12i-a). The local surface cooling modifies the large-scale

meridional distribution of SST and thus enhances the SST front (Fig. 12ii) through heat flux change, in addition to Ekman-convergence (Fig. 12i-b). Then, beside of the vertical shear increased by the enhanced STCC (Fig. 12iii-a), the pycnocline is lifted up in association with the shoaling upper layer (Fig. 12iii-b), which is favorable for the growth of baroclinic instability and enhancement of the eddy growth rate. Thus, the eddies tend to be more active during the negative phases of WP pattern than the positive phases, resulting from the upper-layer shoaling and the enhanced vertical shear strengthening of the STCC-NEC system. This process is directly connected to the Kuroshio-eddies interaction on interannual timescales (Shen et al., 2014). In general, eddies are strengthened as they move westward into a shallower upper-layer region (Fig. 12iv) due to the upper-layer shoaling that is favorable for the instability growth.

Finally, we want to point out that the SST meridional gradient related to the WP pattern studied here could affect the East Asia Winter Monsoon (EAWM), which is sensitive to SST variability (or SST gradient) in the western North Pacific (Wang et al., 2000; Hsu et al., 2001; Liu et al., 2005; Sakai and Kawamura, 2009; Ha et al., 2012; Chen et al., 2013). The ocean-atmosphere interaction through surface heat flux modified by SST modulates the strength of the EAWM (Hsu et al., 2001). The SST cooling strengthened by northeasterly winds can sustain anomalous anticyclonic wind (Wang et al., 2000), which corresponds to a weak EAWM and persists from winter to the following summer (Chen et al., 2013). Moreover, using a coupled ocean-atmosphere model framework, Liu et al. (2005) found that the SST gradient can strengthen and sustain the EAWM. Thus, the SST variability associated with the WP pattern is not only a single event but could be an important ocean-atmosphere interaction for the climate in East Asia.

References

Chelton, D.B., Schlax, M.G., Samelson, R.M., 2011. Global observations of nonlinear mesoscale eddies. Prog. Oceanogr. 91, 167–216.

Chen, W., Feng, J., Wu, R., 2013. Roles of ENSO and PDO in the link of the East Asian winter monsoon to the following summer monsoon. J. Clim. 26, 622–635.

Chow, C.H., Liu, Q., 2012. Eddy-advective effects on the temperature and wind speed of the sea surface in the Northwest Pacific Subtropical Countercurrent area from satellite observations. Int. J. Remote Sens. 34, 600–612.

Chow, C.H., Liu, Q., Xie, S.-P., 2015. Effects of Kuroshio intrusions on the atmosphere Northeast of Taiwan Island. Geophys. Res. Lett. 42, 1465–1470.

Cushman-Roisin, B., Beckers, J., 2008. Introduction to geophysical fluid dynamics–physical and numerical aspects. Academic Press, New Hampshire, USA, 755.

Cushman-Roisin, B., Tang, B., Chassignet, E.P., 1990. Westward motion of mesoscale eddies. J. Phys. Oceanogr. 20, 758–768.

Dee, D.P., et al., 2011. The ERA-Interim reanalysis: configuration and performance of the data assimilation system. Q. J. R. Meteorol. Soc. 137, 553–597.

Ducet, N., Le Traon, P.Y., Reverdin, G., 2000. Global high-resolution mapping of ocean circulation from TOPEX/Poseidon and ERS-1 and -2. J. Geophys. Res. 105 (19), 477–498.

Guinehut, S., Coatanoan, C., Dhomps, A.-L., Le Traon, P.-Y., Larnicol, G., 2009. On the use of satellite altimeter data in Argo quality control. J. Atmos. Ocean. Technol. 26, 395–402.

Ha, K.-J., Heo, K.-Y., Lee, S.-S., Yun, K.-S., Jhun, J.-G., 2012. Variability in the East Asian monsoon: a review. Meteorol. Appl. 19, 200–215.

Hsin, Y.-C., Wu, C.-R., Shaw, P.-T., 2008. Spatial and temporal variations of the Kuroshio east of Taiwan, 1982–2005: a numerical study. J. Geophys. Res. 113, C04002. http://dx.doi.org/10.1029/2007JC004485.

Hsu, H.-H., Chen, Y.-L., Kau, W.-S., 2001. Effects of atmosphere-ocean interaction on the interannual variability of winter temperature in Taiwan and East Asia. Clim. Dyn. 17, 305–316.

Hwang, C., Wu, C., Kao, R., 2004. TOPEX/Poseidon observations of mesoscale eddies over the subtropical countercurrent: kinematic characteristics of an anticyclonic eddy and a cyclonic eddy. J. Geophys. Res. 109 (C8). http://dx.doi.org/10.1029/2003JC002026.

Kazmin, A.S., Rienecker, M.M., 1996. Variability and frontogenesis in the large-scale oceanic frontal zones. J. Geophys. Res. 101, 907–921.

Kobashi, F., Xie, S.-P., 2012. Interannual variability of the North Pacific subtropical countercurrent: role of local ocean-atmosphere interaction. J. Oceanogr. 68, 113–126.

Lin, X., Wu, D., Lan, J., 2006. The analysis of intraseasonal long Rossby wave speed in the subtropical Pacific Ocean. J. Hydrodyn. Ser. B 18, 55–62.

Liu, L., Zheng, Z., Xia, Y., Wu, H., 2005. A primary study of interaction between monsoon and sea surface temperature in the neighborhood sea area in South Asia. Acta Meteorol. Sin. 19, 366–374.

Liu, Q., Li, L., 2007. Baroclinic stability of oceanic Rossby wave in the North Pacific subtropical eastwards countercurrent. Chin. J. Geophys. 50, 84–93.

Nakamura, H., Kazmin, A.S., 2003. Decadal changes in the North Pacific oceanic frontal zones as revealed in ship and satellite observations. J. Geophys. Res. 108 (C3), 3078. http://dx.doi.org/10.1029/1999JC000085.

Qiu, B., 1999. Seasonal eddy field modulation of the North Pacific Subtropical Countercurrent: TOPEX/Poseidon observations and theory. J. Phys. Oceanogr. 29, 2471–2486.

Qiu, B., Chen, S., 2005. Eddy-induced heat transport in the subtropical North Pacific from Argo, TMI, and altimetry measurements. J. Phys. Oceanogr. 35, 458–473.

Qiu, B., Chen, S., 2010. Interannual variability of the North Pacific subtropical countercurrent and its associated mesoscale eddy field. J. Phys. Oceanogr. 40, 213–225.

Qiu, B., Chen, S., 2013. Concurrent decadal mesoscale eddy modulations in the Western North Pacific subtropical gyre. J. Phys. Oceanogr. 43, 344–358.

Qu, T., 2003. Mixed layer heat balance in the western North Pacific. J. Geophys. Res. 108 (C7), 3242. http://dx.doi.org/10.1029/2002JC001536.

Roden, G.I., 1975. On North Pacific temperature, salinity, sound velocity and density fronts and their relation to the wind and energy flux fields. J. Phys. Oceanogr. 5, 557–571.

Roemmich, D., Gilson, J., 2001. Eddy transport of heat and thermocline waters in the North Pacific: a key to interannual/decadal climate variability? J. Phys. Oceanogr. 31, 675–687.

Sakai, K., Kawamura, R., 2009. Remote response of the East Asian winter monsoon to tropical forcing related to El Niño-Southern oscillation. J. Geophys. Res. 114, 06105. http://dx.doi.org/10.1029/2008JD010824.

Shen, M.-L., Tseng, Y.-H., Jan, S., Young, C.-C., Chiou, M.-D., 2014. Long-term variability of the Kuroshio transport East of Taiwan and the climate it conveys. Prog. Oceanogr. 121, 60–73.

Sheu, W.-J., Wu, C.-R., Oey, L.-Y., 2010. Blocking and westward passage of eddies in the Luzon Strait. Deep-Sea Res. II 57, 1783–1791.

Small, R.J., Xie, S.P., Hafner, J., 2005. Satellite observations of mesoscale ocean features and co propagating atmospheric surface fields in the tropical belt. J. Geophys. Res-Oceans, *110*, C02021, doi:10.1029/2004JC002598.

Vélez-Belchí, P., Centurioni, L.R., Lee, D.-K., Jan, S., Niiler, P.P., 2013. Eddy induced Kuroshio intrusions onto the continental shelf of the East China Sea. J. Mar. Res. 71, 83–107.

Wallace, J.M., Gutzler, D.S., 1981. Teleconnections in the geopotential height field during the Northern hemisphere winter. Mon. Weather Rev. 109, 784–812.

Wang, B., Wu, R., Fu, X., 2000. Pacific–East Asian teleconnection: how does ENSO affect East Asian climate? J. Clim. 13, 1517–1536.

Wu, R., Kirtman, B.P., Pegion, K., 2006. Local air-sea relationship in observations and model simulations. J. Clim. 19, 4914–4932.

Yang, G., Wang, F., Li, Y., Lin, P., 2013. Mesoscale eddies in the northwestern subtropical Pacific Ocean: statistical characteristics and three-dimensional structures. J. Geophys. Res. Oceans, *118*. http://dx.doi.org/10.1002/jgrc.20164.

Yang, Y.1999. Mesoscale eddies' influence on the Taiwan Current (Kuroshio) volume transport, pH.D. thesis, Inst. of Oceanogr., Natl. Taiwan Univ., Taiwan.

Yuan, D., Han, W., Hu, D., 2006. Surface Kuroshio path in the Luzon Strait area derived from satellite remote sensing data. J. Geophys. Res. Oceans 111, C11007, doi:10.1029/2005JC003412.

Zhang, D., Lee, T.N., Johns, W.E., 2001. The Kuroshio east of Taiwan: modes of variability and relationship to interior ocean mesoscale eddies. J. Phys. Oceanogr. 31, 1054–1074.